International Journal of Hydrogen Energy 136 (2025) 663–671

Contents lists available at ScienceDirect

International Journal of Hydrogen Energy

journal homepage: www.elsevier.com/locate/he

Effect of hydrogen on the temperature-dependent activation volume and the strain rate sensitivity of structural steel, coarse-grained and nanocrystalline Nickel

Florian Schaefer *, Lukas Hasenfratz, Rouven Schneider, Christian Motz

Materials Science and Engineering, Saarland University, Campus D2 3, Saarbruecken, 66123, Saarland, Germany

ARTICLE INFO

Keywords:
Strain rate sensitivity
Activation volume
Strain rate jump tensile test

ABSTRACT

For more than 150 years, it has been considered proven that hydrogen generally degrades the mechanical performance of metals. Nevertheless, there is no consensus on the exact mechanisms, how hydrogen affects plastic deformation. The strain rate sensitivity of a material results from a thermally activated contribution to the rate-determining deformation process, e.g. to dislocation slip or dislocation grain boundary interaction. In this study, the extent to which hydrogen affects thermally activated dislocation motion and hence the strain rate sensitivity was investigated. For this purpose, specimens were cathodically charged *in situ*, and subjected to nanoindentation. In addition, macro-tensile tests with strain rate jumps were performed varying the temperature into the cryogenic range, to inhibit effusion, but also to test the effect of hydrogen on the activation parameters of deformation. Hydrogen was shown to increase the strain rate sensitivity of f.c.c. nickel, whereas it is not affected for a structural steel with a b.c.c. lattice. The activation volume for plastic deformation in a direct comparison between nanocrystalline and coarse-grained f.c.c. nickel and the b.c.c. structural steel shows, that the rate-determining deformation mechanism appears to change for f.c.c. but not for the b.c.c. material.

1. Introduction

When W. H. Johnson found in 1875 that steel lost both ductility and strength after exposure to hydrogen [1], this phenomenon quickly became known as *Hydrogen Embrittlement (HE)*. Although Johnson already knew that effusion annealing removes hydrogen from the material, the history of damage caused by hydrogen is long. Approaches to explaining this degradation of material performance are either more phenomenological, as in the case of *Hydrogen-induced Cracking (HIC)* [2–4] or mechanistic as i. a. in the case of *Hydrogen-enhanced Decohesion (HEDE)* [5,6], *Hydrogen-enhanced Localized Plasticity (HELP)* [7] or the *defactant* theory by R. Kirchheim [8–10]. However, experimental results range from a softening [11–14] to hardening [15] of the material, in particular the latter by a Cottrell-like hydrogen atmosphere around dislocations [16,17], depending on the temperature [18] and the hydrogen concentration [19,20]. In addition to the degradation of ductility and strength, hydrogen can also lead to an increase in the mechanical performance in some materials under certain conditions [21–23].

How hydrogen actually affects the material behavior depends, among other things, on the material itself and its deformation mechanisms (crystal structure such as b.c.c. or f.c.c., with their specifics for dislocation mobility and the grain size), on the hydrogen charging method, i.e. on the hydrogen content and its distribution ("high-fugacity" (electro-)chemical or "low-fugacity" charging from the gas phase [24]), on the loading rate (e.g. the necessity for slow strain rate testing) [25] and on the loading case (e.g. homogeneous tensile testing or crack growth). This interplay is complex and, even after 150 years, is only just beginning to be understood. That hydrogen has an effect on the strain rate sensitivity of a metal is made clear not only by the well-known fact that the test speed in slow strain rate testing significantly affects the test results [26,27], but among others also by the fact that hydrogen interacts with those material defects that determine the plasticity of materials. For example, hydrogen attaches to the dislocation core [28] and can relax it or to the stress field of dislocations, where hydrogen significantly influences their interaction with grain boundaries [16,29].

Hydrogen also modifies dislocation nucleation and motion. Particularly in f.c.c. metals, a more planar, localized slip is observed by slip traces on the surface of the specimen [23,30,31]. Even if the underlying reasons are still under discussion, it can be assumed

* Corresponding author.
E-mail addresses: f.schaefer@matsci.uni-sb.de (F. Schaefer), f.schaefer@matsci.uni-sb.de (C. Motz).
URL: https://www.uni-saarland.de/mww (F. Schaefer).

https://doi.org/10.1016/j.ijhydene.2024.06.343
Received 31 January 2024; Received in revised form 11 June 2024; Accepted 25 June 2024
Available online 8 July 2024

that hydrogen significantly affects the interaction of dislocations with barriers and forest dislocations [16]. In b.c.c. systems, the mobility of screw dislocation segments is the rate-limiting process during plastic deformation [32]. The competing hydrogen effects of softening by lowering the kink nucleation enthalpy [33] and hardening by pinning the kink migration depend on temperature, stress level, other impurities (such as C in steel compared to pure iron) and the strain rate [18]. In kink migration, hydrogen has been shown to manipulate both, the secondary Peierls potential as well as the primary one for kink nucleation. Thermal activation is required to overcome the secondary Peierls potential in the presence of hydrogen [18–20]. In contrast to f.c.c. and the hydrogen-free state in the b.c.c. system, kink migration becomes the rate-determining step. Thus, a strain rate sensitivity depending on the hydrogen concentration evolves [20]. To date, these findings have largely been based on atomistic simulations. Wang et al. [34] showed in relaxation experiments in pure iron and iron alloys containing 8 and 7.71 wt% Cr that the activation volume V^* tends to decrease and thus the strain rate sensitivity m tends to increase with a higher hydrogen concentration, i.e. the thermal activation increases by hydrogen. In pure iron, after a steep decrease when H is added, V^* remains at a plateau of $170\ b^3$ for charging currents between 5 and 35 mA/cm^2, which means up to 20 appm hydrogen concentration. In the iron alloys the activation volume decreases without a plateau with increasing H content. For the maximum charging current tested in this study. We have tried to interpret rather than describe the results of Wang et al. Therefore, instead of the charging current, we converted directly to the hydrogen concentration using their Fig. 2. In some cases, however, the presentation was not specific enough. We have revised and sharpened the presentation. We thank the reviewer for this feedback., the activation volume drops below $50\ b^3$. This was interpreted on the basis of a competition between the pinning of dislocations by hydrogen and the increased mobility of hydrogen through the HELP mechanism. Varying the test temperature from room temperature up to 70 °C revealed a reduction of the activation enthalpy ΔH^* of about 10% for pure iron whereas it remained constant for the alloys. They attributed this to an solute solution effect of the additional alloying elements and precipitates in the context of the HELP mechanism. For coarse grained and pre-charged f.c.c Ni, Sirois et al. [35] also found a decrease of V^* in relaxation tests in the presence of an intermediate hydrogen concentration and concluded based on a constant flow stress gradient over temperature $\frac{d\sigma_f}{dT} = const.$ that the activation enthalpy is lowered by a decrease of the activation volume and thus the dislocation velocity increases due to hydrogen. They interpreted these results in terms of the HELP mechanism. This reduction in V^* with increasing hydrogen concentration was also found by Abraham et al. in SAE 310S austenitic stainless steel highly saturated with hydrogen by strain rate jump tensile tests and stress relaxation tests [30].

How hydrogen interacts with the slip mechanisms leaves a fingerprint in the thermal activation parameters, i.e. the strain rate sensitivity and the activation volume. In principle, both parameters allow to deduce the deformation processes that take place on the atomic scale.

This study is dedicated to the question of the extent to which an intermediate hydrogen concentration affects the deformation mechanism. The direct comparison of coarse and nanocrystalline nickel with a grain size below 40 nm from pulsed electro-deposition [36] is used to investigate how the interaction of grain boundaries and dislocations changes as a result of hydrogen exposure. At the same time, the significant differences in the hydrogen effect on the deformation behavior between a pure f.c.c. material and a technical b.c.c. alloy, a structural steel, are investigated.

2. Thermodynamical and experimental background

In principle, thermal activation parameters can be obtained from relaxation, creep and strain rate jump tests. It is essential that the internal microstructure of the material, in particular the dislocation density, remains constant when determining the derivatives shown below. For this reason, tests with varying mircostructure or dislocation density such as creep tests as well as at different strain rates and their comparison tend to give deviating results [37,38]. Although the use of transient methods to determine the activation parameters also causes changes in the dislocation configuration, which become visible as transients between the strain rate jumps [39], this technique has proven itself in practice. The same applies to stress relaxation tests, where the dislocation density generally decreases during relaxation [40].

The strain rate sensitivity m is given by

$$m = \frac{\partial \ln \sigma_f}{\partial \ln \dot{\varepsilon}} \tag{1}$$

as the exponent in the power-law relation between the strain rate $\dot{\varepsilon}$ and the flow stress σ_f.

Assuming a fixed Gibbs activation enthalpy ΔG^* for a deformation process, the strain rate is given by

$$\dot{\varepsilon} = \dot{\varepsilon}_0 \cdot \exp\left(\frac{-\Delta G^*}{k_B T}\right) \tag{2}$$

with the Boltzmann constant k_B and a pre-exponential factor $\dot{\varepsilon}_0$. If an external shear stress τ consisting of an athermal and a thermal part $\tau = \tau_{ath} + \tau_{th}$ is applied, the effective shear stress τ_{th} reduces the activation enthalpy compared to the activation enthalpy necessary at zero stress ΔG_0^*.

$$\Delta G^* = \Delta G_0^* - \tau_{th} \cdot V^* \tag{3}$$

The activation volume $V^* = b \cdot A^*$ can be considered as the volume arising from the Burgers vector b and the area A^* swept out by a dislocation segment between a stable equilibrium position in the Peierls potential to the next one, which means the area around an obstacle according to the Seeger model [41,42].

In order to derive the activation volume experimentally the following conversions starting from

$$V^* = -\frac{\partial \Delta G^*}{\partial \tau_{th}} \tag{4}$$

with Eq. (2) following

$$V^* = k_B T \left(\frac{\partial \ln \dot{\varepsilon}}{\partial \tau_{th}} - \frac{\partial \ln \dot{\varepsilon}_0}{\partial \tau_{th}}\right) \tag{5}$$

with

$$\partial \frac{\ln \dot{\varepsilon}_0}{\partial \tau_{th}} = 0 \tag{6}$$

following

$$V^* = k_B T \frac{\partial \ln \dot{\varepsilon}}{\partial \tau_{th}} \tag{7}$$

$$\Rightarrow V^* = k_B T \frac{\partial \ln \dot{\varepsilon}}{\partial \sigma_f} \cdot \frac{\partial \sigma_f}{\partial \tau_{th}} \tag{8}$$

leading to with the Taylor factor M

$$V^* = k_B T M \frac{\partial \ln \dot{\varepsilon}}{\partial \sigma_f} \tag{9}$$

With the relation shown in Eq. (10), the connection between activation volume V^* and strain rate sensitivity m can be derived, which is shown in Eq. (11).

$$\frac{1}{m} = \frac{\partial \ln \dot{\varepsilon}}{\partial \ln \sigma_f} = \frac{\partial \ln \dot{\varepsilon}}{\partial \sigma_f} \cdot \left(\frac{\partial \ln \sigma_f}{\partial \sigma_f}\right)^{-1} = \frac{\partial \ln \dot{\varepsilon}}{\partial \sigma_f} \cdot \sigma_f \tag{10}$$

$$V^* = M \frac{k_B T}{m \cdot \sigma_f} \tag{11}$$

If the von Mises yield criterion is used in the case of nanoindentation instead of the Taylor relation for uniaxial test, M is set to $\sqrt{3}$. For nanoindentation the flow stress σ_f is replaced by the hardness H_{NI} using the Tabor relation $H_{NI} = 3\sigma_f$ [38]. The activation enthalpy can

be determined assuming that $\frac{\partial \ln \varepsilon_0}{T} = 0$ by measuring the strain rate sensitivity from strain rate jump tests at different temperatures by

$$\Delta H^* = -k_B T^2 \cdot \frac{\partial \ln \dot{\varepsilon}}{\partial \sigma_f} \cdot \frac{\partial \sigma_f}{\partial T} = \frac{k_B}{m} \cdot \frac{\partial \ln \sigma_f}{\partial T^{-1}} \quad (12)$$

Strain rate jump tests (SRJTs) are very well established in nanoindentation [43–45], especially for the investigation of nanocrystalline materials [38,46], and has already been used to investigate the hydrogen-induced increase in strain rate sensitivity and the corresponding decrease of the activation volume of a nickel-based superalloy [31]. The stiffness of the system is measured continuously during indentation using the so-called "continuous stiffness method" (CSM) and the hardness and the indentation modulus are determined from the indentation depth h and from the contact stiffness. A constant strain rate could be achieved by controlling the loading rate as shown in Eq. (13) [43,46,47]. It is assumed that a self-similar indenter leads to a radius of the deformation field e.g. the plastic zone underneath the indenter tip that scales with the radius of the contact area A_C and thus the indentation depth h respectively. Hence, the strain rate $\dot{\varepsilon}$ is proportional to the evolution of the contact area $\dot{A_C}$ and the indentation depth $\dot{h}$ [43]. As the hardness H is derived from $\frac{P}{A_C}$ with $A_c \propto h^2$, differentiation leads to

$$\dot{\varepsilon} = \frac{\dot{h}}{h} = \frac{1}{2}\left(\frac{\dot{P}}{P} - \frac{\dot{H}}{H}\right) \approx \frac{\dot{P}}{P} \quad (13)$$

SRJTs in nanoindentation have the advantage that m is probed at one indentation without changing the position on the specimen and jump testing provides a constant microstructure as already discussed above. This eliminates the artifacts associated with constant strain rate (CSR) testing and comparing results from different indentations at different strain rates. In addition, the ability to compare a large number of measurements from a small amount of material makes nanoindentation very efficient.

Strain rate jump testing during a tensile test has obviously the general advantage that the strain rate sensitivity is obtained as a function of the strain at which the strain rate jumps occur [42]. In nanoindentation, the average indentation strain is constant for a specific pyramidal indenter, for example ≈8% for a Berkovich indenter [48]. Using a spherical indenter to vary the indentation strain during indentation is complex in combination with strain rate jump testing [49] and tends to suffer from artifacts. Although a real Berkovich indenter is never perfectly self-similar because it is always rounded at the tip, this test geometry comes closer to the assumptions of Eq. (13), especially for a larger indentation depth, and has proven itself in practice. Therefore, spherical indentation is not part of this investigation.

3. Experimental methods

Strain rate jump testing in tension is combined with nanoindentation. The latter becomes necessary when material from HE to such an extent that tensile testing is no longer possible because the residual plasticity has disappeared. In this case, it is evidently no longer possible to evaluate the strain rate sensitivity from jumps in the plastic regime of the stress–strain curve. However, *in situ* charging with hydrogen is hard to combine with nanoindentation at cryogenic temperatures. Thus, both methods are combined here.

3.1. In situ electrochemical testing - Effects of charging method

In principle, there are two different charging strategies for hydrogen: from the gas phase, ideally under high pressure and/or temperature, or electrochemically. High-pressure gas charging is often referred to as "low fugacity charging" because hydrogen comes close to the ideal gas state, especially at high temperatures, and has a comparatively low chemical potential to penetrate into the material even at high pressures in direct comparison to the high activity in electrochemical charging, which can be referred to as "high fugacity charging". Only the latter is practically feasible for nanoindentation. Thus, in contrast to gas-phase charging, the hydrogen concentration usually obtained with electrochemical charging is high and thus prevents hydrogen effusion during non *in situ* charging during testing. Hence, electrochemical charging was used in this study. This will of course be accompanied by a strong gradient of the hydrogen concentration from the surface to the bulk [50], which can only be compensated for by aging with simultaneous outgassing. Studies on this are rare and complex to perform, so that finite element simulations are usually used [51], i.a. to identify a charging time and current to achieve a steady state hydrogen concentration an distribution.

During the *in situ* electrochemical nanoindentation (EC-NI), the membrane-like specimens were loaded from the backside with the setup shown in [52] in order to avoid both extremely high hydrogen concentrations on the surface, as they occur during EC-NI in the electrochemical cell and would not be comparable to bulk behavior, and to avoid a corrosive surface change during the measurements. The tensile tests were carried out in a bath cryostat to lower the temperature stepwise. As cryogenic testing significantly reduces hydrogen effusion, the specimens were electrochemically pre-charged and tested without *in situ* charging. The time between removal from the charging and completion of the tensile test was always less than 60 min, so that no significant effusion was to be expected. The charging times were selected for both the nanoindentation and the tensile tests in such a way that intermediate up to high hydrogen concentrations are expected.

3.2. Material selection

A ferritic-pearlitic structural steel S235JR is used as a typical representative of a b.c.c. low carbon steel with its plastic deformation behavior dominated by the mobility of $<\bar{1}11>$-screw dislocations on {110}-slip planes. The mean grain size was checked by metallographic polishing with a final silica polishing and optical microscopy to 30–50 μm. For representative f.c.c. materials with $<\bar{1}10> - \{111\}$-slip a coarse and a nanocrystalline Nickel was chosen. The latter was produced by pulsed electro-deposition. All specimens were from the same batch to avoid variations in the microstructure and hence the mechanical performance from that. The mean grain size, checked by EBSD and TEM, was less than 40 nm. For more information, see [36,53]. The coarse-grained Nickel was produced from 99.995% high-purity nickel (Goodfellow Cambridge Ltd., Huntingdon (UK)) and heat treated for 18 h at 1100 °C in a vacuum better than 10^{-5} mbar. The mean grain size could be checked afterwards by optical microscopy due to the thermal etching and was larger than 50 μm.

3.3. Strain rate jump tests

Tensile testing. The electrolyte used for pre-charging was prepared from 1.3 M $Na_2B_4O_7 \cdot 10\,H_2O$ (borax, VWR Avantor Inc., USA) in glycerol anhydrous for synthesis (Merck KGaA, Darmstadt, GER) mixed with double-distilled water (VWR Avantor Inc., USA) with a volume ratio of 4:1 [54]. As a recombination poison, 1 g/l $Na_2S_2O_3$ (sodium thiosulphate, VWR Avantor Inc.) is added. To reduce the high viscosity of the glycerol, prevent precipitation of the borax and facilitate mixing with the distilled water, the electrolyte was heated to 55 °C during charging and stirred at 100 rpm. Charging was carried out galvanostatic with a current density of 1 mA/cm^2. A charging time of 168 h was selected for the nickel specimens and 23 h was selected for the steel specimens due to the significantly higher diffusion rate in b.c.c. materials.

Specimens were manufactured by spark erosion (EDM) according to ISO 10002 with a gauge length of 10 mm, a parallel length of 12 mm and a radius of 6 mm. The specimen cross section was 2.5 mm × 1 mm. Specimens were ground to remove material affected by EDM. Tests were performed on a servo-hydraulic testing machine Instron 8511 with a EDC580 controller from Doli, Germany. The specimens

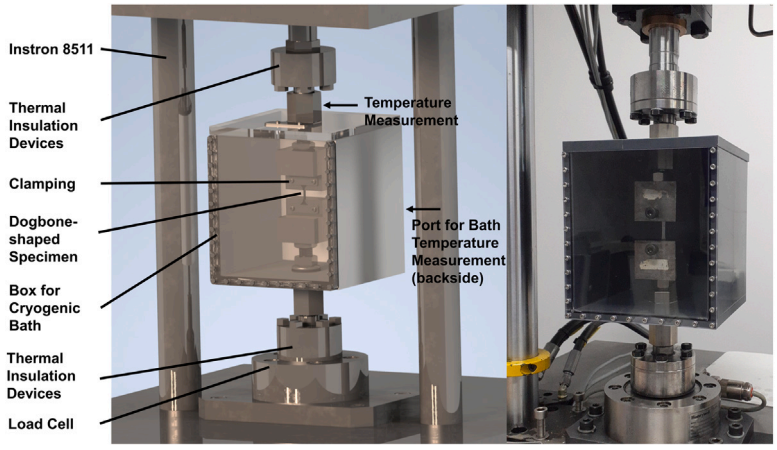

Fig. 1. Schematic of the cryogenic bath at the Instron 8511 tensile testing machine and photograph without cooling agents and Pt1000 sensors (1-column figure).

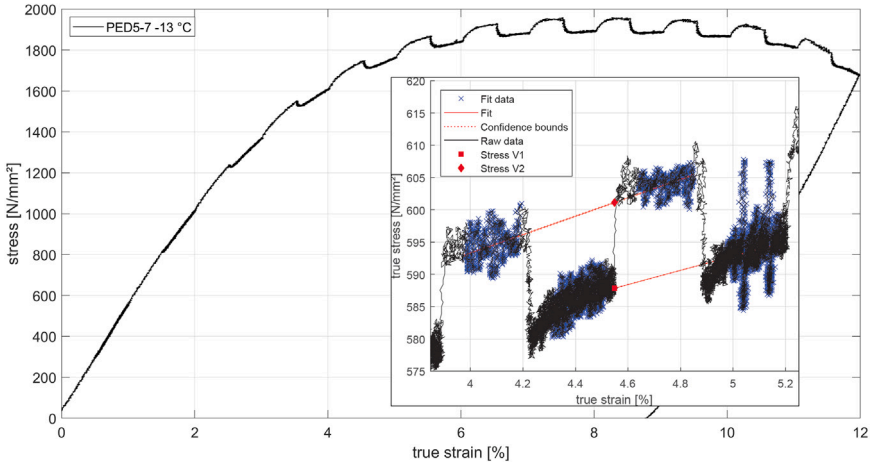

Fig. 2. True stress vs. true strain curve from nc-Ni from PED, measured at −13 °C; the inset shows the data analysis by segment-wise fitting of data after clean-up: the strain rate sensitivity for the specific jump and thus true strain follows from Stress V1 and Stress V2 (1.5-column figure).

Table 1
Cryogenic baths and cooling agents.

Cooling agent	Temperature [°C]
H_2O_l + H_2O_s	0
$C_2H_6O_2$ (ethyleneglycol) + dry ice	−15
$1\,H_2O_s + 3\,NaCl$	−20
$1\,H_2O_s + 0.8\,(CaCl_2 \cdot 6\,H_2O)$	−40
C_2H_6O (acetone) + dry ice	−78

were mounted with form-fitting clamps and tested at room temperature as well as immersed in a cryogenic bath, see Fig. 1. The temperatures and the composition of the bath are given in Table 1. Prior to each test, the specimen was held in the bath until the temperature gradient along the clamping was constant, measured with a Pt1000 resistance thermometer, as was measured the bath temperature. Due to the test setup and the cooling agents used, it was not possible to carry out strain measurements using a tactile extensometer, strain gauges or a video extensometer. The strain determined here is therefore based on the change in the crosshead position of the testing machine. The ratio between the crosshead displacement and the strain in the measuring range, which is influenced by the specimen shape and its stiffness as well as by the hardening behavior, was previously calibrated for each material using a clip-on extensometer (634, 31E-24, MTS Systems Corporation, USA).

An experimental control program was written as C code for the tensile strain rate jump tests. After an initial strain of 0.5% segments with a corresponding strain of less than 0.5% were applied. Strain rate sensitivity and the activation volume were measured from strain rate jumps of factor 10 from 10^{-2} 1/s and evaluated from the true stress vs. true strain curve using MATLAB, see Fig. 2.

Nanoindentation. Nanoindentation tests had to be performed to determine the strain rate sensitivity and the activation volume for the nanocrystalline nickel, because hydrogen embrittlement occurred after charging and the plastic ductility approached almost zero. The tests were carried out at room temperature on a Hysitron TI900 with Performech 2 controller, equipped with *nanoDMA* and a 10 mN standard transducer. For this purpose, a load function was generated using a C code. The strain rate was varied between 0.1 1/s and 0.001 1/s. The specimens were first galvanostatically pre-charged for 2 days in an electrolyte of 1M H_2SO_4 + 5 g/l KI at 1 mA/cm^2 and then further charged and tested in the *in situ* setup, explained and shown in [52], because a lower viscosity of the electrolyte is needed for this specific setup. Since an approximately 100 µm thick membrane is tested here, special attention must be paid to the machine compliance calibration, even if an error in this offset would level out to a large extent due to the evaluation by the strain rate jumps. Preliminary, the SRJT method was preliminary tested on bulk coarse-grained (and thus single crystalline for nanoindentation) and nanocrystalline nickel. The results from SRJTs and constant strain rate tests (CSR) were compared and no remarkable difference in the measured strain rate sensitivity was found (m_{SRJT} = 0.017, m_{CSRT} = 0.018), see Fig. 3.

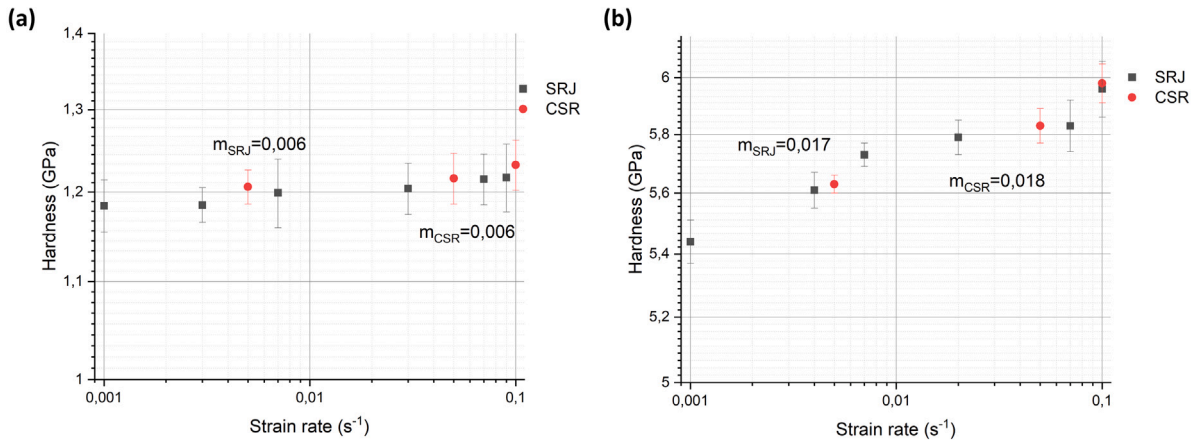

Fig. 3. Comparison of measured hardness from nanoindentation for (a) single crystalline Ni and (b) nanocrystalline Ni; the strain rate sensitivity is the slope of the regression line and the corresponding values for the constant strain rate (CSR) and strain rate jump tests (SRJT) are shown (2-column figure).

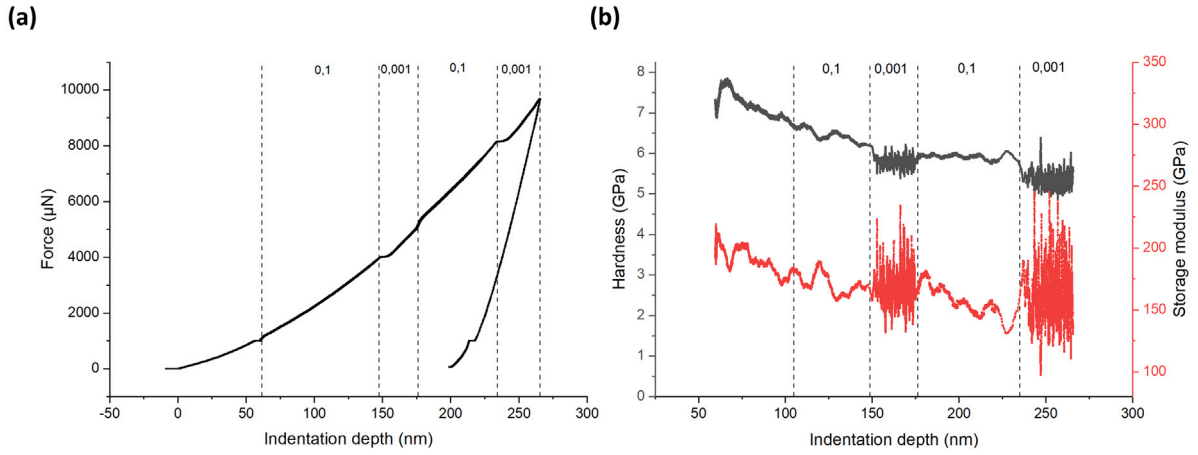

Fig. 4. Strain rate jump test by nanoindentation for H charged nc-Ni (a) the load displacement curve shows a typical drop in the load when the strain rate drops and (b) hardness (black) and indentation modulus (black) from CSM (2-column figure).

4. Results

Fig. 4 shows that hardness jumps coincide with strain rate jumps while the indentation modulus is not affected by the strain rate jump, as expected (besides a larger scattering originating from the larger number of data points in the slower segments). The resulting evolution of the strain rate sensitivity m as a function of the temperature of the cryostatic bath, determined from a jump of strain rate at 4% true strain in the tensile tests, is shown in Fig. 5a–d. For nanocrystalline Ni from PED the results in Fig. 5a are in good agreement with those obtained by Maier et al. [38]. The strain rate sensitivity of Ni decreases with decreasing temperature, although there is just an increase in the flow stress of about 10% between 0 and −62 °C. In contrast to cg-Ni and S235JR steel m increases as a function of the true strain. As an increase in m is generally attributed to a activation volume V^* that tends to decrease and *vice versa* it can be assumed that lowering the temperature leads to a larger volume required to activate deformation. This is due in particular to the fact that plastic deformation in nc materials is caused by the interaction of dislocations and partial dislocations with grain boundaries and by grain boundary sliding processes [55]. It is assumed that these are more difficult at lower temperatures, so that a larger volume must be activated for cooperative movement in order to absorb and release or transfer dislocations or to relax grain boundaries in the course of the interaction. A decrease in the activation volume with strain might be an effect of grain boundary relaxation in the course of plastic deformation, although this is unintuitive. However, the structure of the grain boundary might relax to become more susceptible to further deformation. This should be further examined in future studies. The strain rate sensitivity of nc-Ni determined from nanoindentation (see Figs. 3 and 4) with 0.017 and 0.018 at room temperature also in good agreement with the results from the tensile tests. When hydrogen is present, as already mentioned above, the ductility disappears and no evaluation of m is possible from tensile testing. Thus, the only data point gathered is from nanoindentation, where the presence of hydrogen causes an increase of m to 0.0265 ± 0.0045.

The strain rate sensitivity of coarse-grained Ni remained unchanged with temperature variation, but is strongly increased for all temperatures tested when hydrogen charging is applied in Fig. 5b. The measured values for m for the uncharged specimens are in good agreement with the literature values [42,56], although these are slightly lower. This can be attributed to differences in the grain size. Dalla Torre et al. [56] used material with larger grain size for strain rate jump tests in tension and Vehoff et al. also used Ni from electro-deposition.

The structural steel S235JR (in Fig. 5c) exhibits no clear change of the strain rate sensitivity m over all tested temperatures. However, the steel specimens exhibt strong increase of m when temperature decreases. This is generally to be expected, as the amount of thermal activation to the flow stress becomes more dominant when the temperature decreases. For both cg-Ni and S235JR m decreases with strain meaning that a larger activation volume is required to overcome obstacles like forest dislocations.

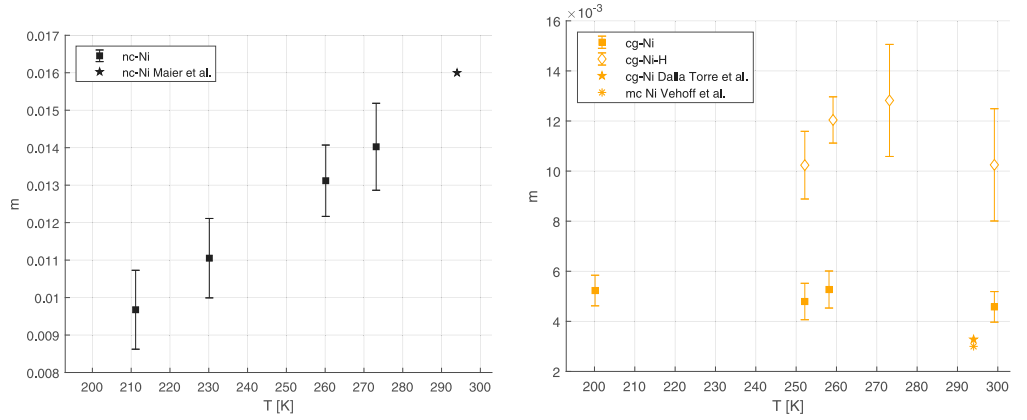

(a) Strain rate sensitivity m of nc-Ni from PED and comparison with data obtained by Maier et al. for nc-Ni from PED [38]

(b) Strain rate sensitivity m of coarse grained-Ni and comparison with data obtained by Dalla Torre et al. [56] and Vehoff et al. [42]

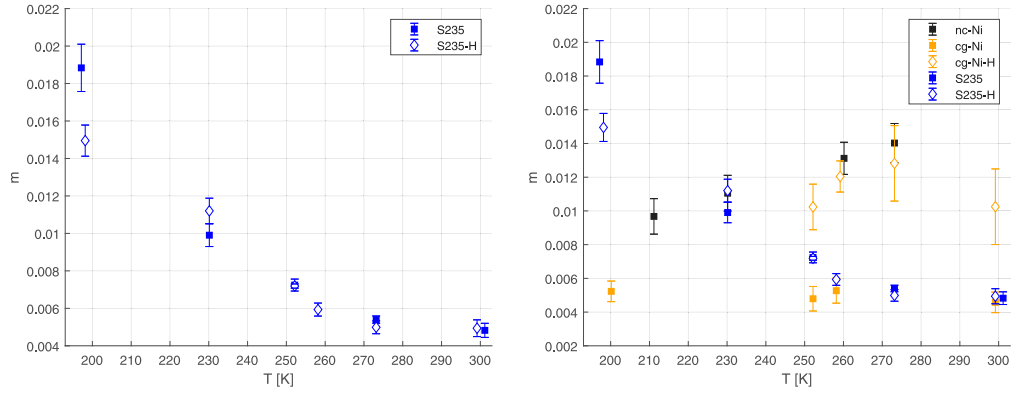

(c) Strain rate sensitivity m of steel S235JR

(d) Comparison of measured strain rate sensitivities

Fig. 5. Measurement results of strain rate sensitivity m, determined from strain rate jump tests in tension, temperature variation by bath cryostat, the suffix -H in the legend (unfilled markers) refers to data with H exposure whereas those with filled markers are from tests without H.

5. Activation volume

The Seeger model [41] for the activation volume V^* is non-intuitive in the sense that the activation volume is not a parameter that impedes activation, similar to the activation enthalpy. Rather, it is the volume that needs to be activated for deformation and thus, if V^* is small, then activation tends to concentrate to smaller region around the defects because the rate-determining deformation process is that in which dislocations interact with obstacles in their immediate vicinity (grain boundaries in nc materials or pinning of the dislocation line by interstitials).

However, slip is not localized in the sense of the HELP mechanism by that although the distance between obstacles for slip decrease. As V^* increases, the obstacle density decreases, as with dislocations interacting with others in a network (forest cutting). The activation volume essentially provides information about the spatial extent of the required activation, i.e. the critical length scale for a deformation mechanism.

According to Eq. (3), the extent of the thermodynamic activation barrier ΔH_0^* also follows from Eq. (12) from the term $\frac{\partial \ln \sigma_f}{\partial T^{-1}}$. However, this term is also determined by the deformation processes, such as the pinning by other interstitials or the Peierls potential itself. The activation volume is just determined by the deformation process and allows for splitting the effects.

However, the magnitude of V^* shown in Fig. 6a–d can be used to infer the nature of the deformation mechanism by its spatial extent, see Fig. 7. A pinning mechanism as the rate-determining process leads to expect very small values of V^*, whereas a reduction in the distance' between dislocations by shielding, as postulated by the HELP mechanism, should also lead to only a slight decrease of V^*. Since both effects tend to the same direction, it is hard to distinguish between both, although the magnitude of V^* gives indication.

For nc-Ni, hydrogen reduces the activation volume to a very small value of $V^* = 2.98b^3$. This shows that the rate-determining deformation process is extremely concentrated to a small region. This indicates a diffusion based deformation process like grain boundary sliding. At the same time, the hardness increases. This is a strong indication that hydrogen affects the slip behavior via a pinning effect, either affecting V^* or ΔH_0^* or both. Together with the hardening it can be assumed that hydrogen does not facilitate the interaction of the dislocations with the grain boundary.

A direct comparison of the temperature response of the activation volume for nc-Ni and coarse-grained nickel shows that the activation volume and thus the rate-determining deformation process is independent of the temperature for nc-Ni, while only a slight temperature dependence can be observed for the hydrogen-free case for coarse-grained nickel. This slight temperature dependence disappears in the presence of hydrogen, so that it can be concluded that hydrogen dominates the rate-determining deformation process also for coarse-grained nickel. The determined activation volume is in good agreement with the data measured by Wang et al. [58].

It must be assumed that the hydrogen effects on the rate-determining deformation processes found here are strongly dependent on the rate of deformation itself. For very high strain rates, it can be

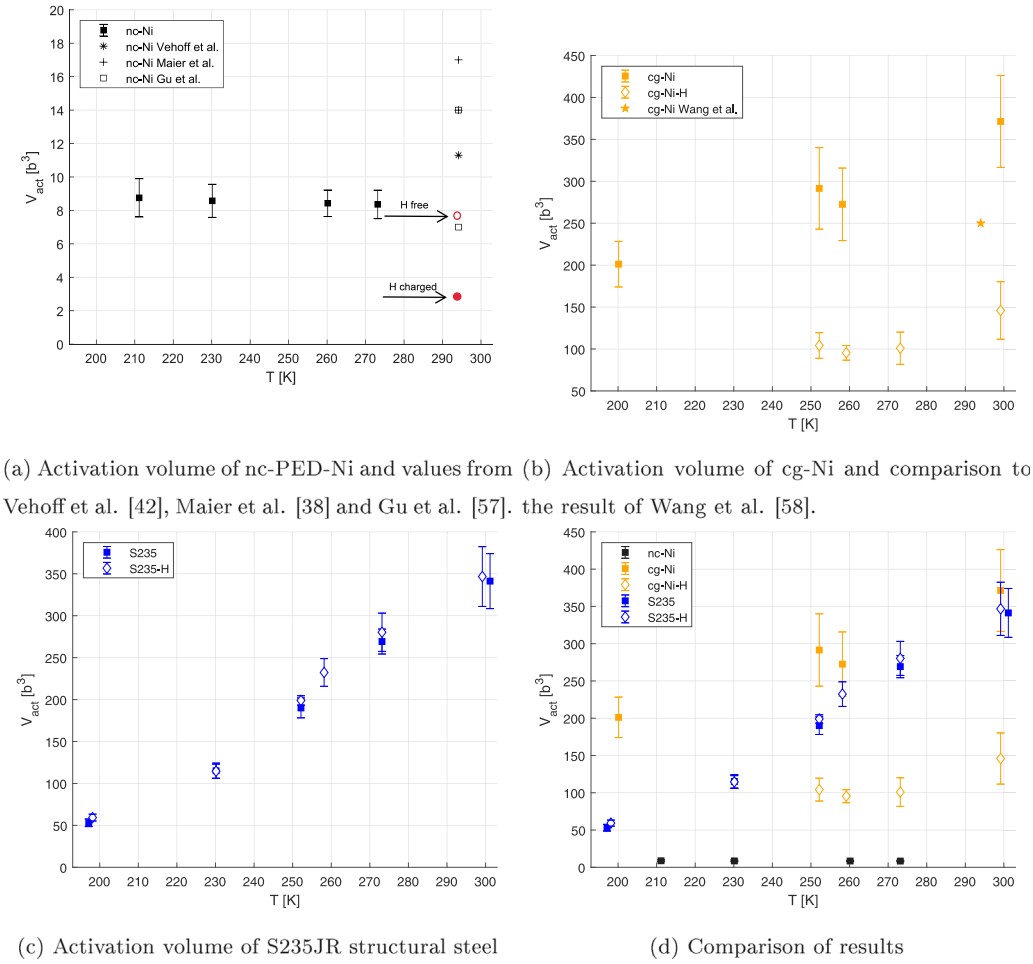

(a) Activation volume of nc-PED-Ni and values from Vehoff et al. [42], Maier et al. [38] and Gu et al. [57].

(b) Activation volume of cg-Ni and comparison to the result of Wang et al. [58].

(c) Activation volume of S235JR structural steel

(d) Comparison of results

Fig. 6. Activation volume, determined from the strain rate sensitivity and the flow stress at 4% true strain. Most results are determined from the tensile SRJTs, the datapoints in red in Subfig. (a) originated from the nanoindentation SRJTs, the suffix -H in the legend (unfilled markers) refers to data with H exposure whereas those with filled markers are from tests without H (see [57]).

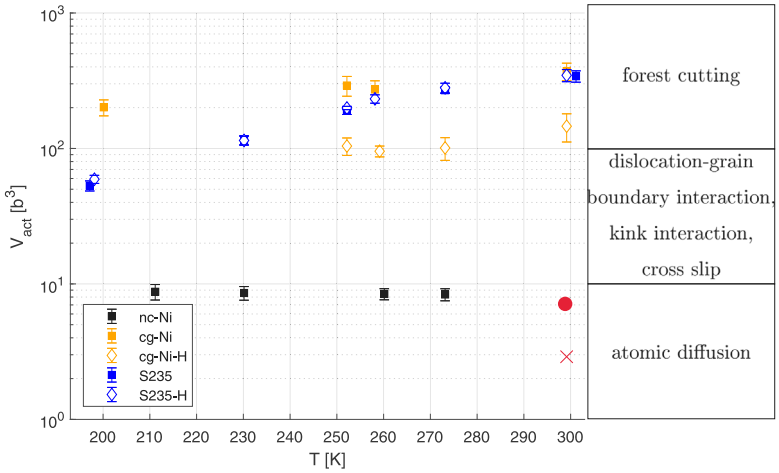

Fig. 7. V^* measured at 4% true strain and information on corresponding typical deformation mechanisms (the red point marks V^* determined by nanoindentation at room temperature for nc-Ni and the red cross the same specimen, charged with hydrogen, also derived from nanoindentation) (1.5 column figure), the suffix -H in the legend (unfilled markers) refers to data with H exposure whereas those with filled markers are from tests without H.

assumed that hydrogen can no longer exert its pinning effect through its limited diffusion velocity [59].

In contrast, the steel S235JR shows no clear effect of hydrogen on the rate-determining deformation process. However, the gradient of V^* over temperature is much more pronounced than for coarse-grained nickel and reflects the stronger thermal activation required in the b.c.c. system. However, no clear pinning effect of hydrogen can be confirmed here, nor an influence of hydrogen on the strain rate sensitivity and the activation volume itself, as described by Gong et al. for pure iron [20]. The pinning effect of carbon seems to overlay the hydrogen effect.

However, it still cannot be ruled out that hydrogen has a direct effect on the Peierls potential. More detailed investigations of ΔH_0^* are required.

6. Conclusion

In this work, the effect of hydrogen on the strain rate sensitivity and the activation volume after electrochemical charging and thus high hydrogen concentration was investigated by varying the test temperature using SRJTs in classical tensile testing and in nanoindentation. The values determined are in good agreement with literature values where these were available. The combination of the methods, the variation of the temperature over such a wide range and the comparison of b.c.c. and f.c.c. materials, the latter with grain sizes in the nano- and coarse grained regime, provides the following main findings:

- H affects the strain rate sensitivity and the activation volume in both, nc- and coarse-grained Ni but not in b.c.c. structural steel.
- In the f.c.c. system, temperature tends to not affect the activation volume, but hydrogen does. Especially for nc-Ni, a pinning effect of hydrogen or a change in the deformation behavior of the grain boundary dominate the rate-determining deformation process. The presence of hydrogen results in a temperature invariant decrease of the activation volume for cg-Ni. Thus, an temperature invariant decrease in the activation enthalpy is expected for nc-Ni, too.
- Structural low carbon steel exhibits, in contrast to pure iron in literature, no change in the activation volume at all tested temperatures by the presence of hydrogen. A change in the activation enthalpy is thus expected from $\frac{\partial \ln \sigma_f}{\partial T^{-1}}$.

In future work, the effect of hydrogen on ΔH_0^* can provide information on how hydrogen interferes with the Peierls potential and, whether the reduction of the activation enthalpy also occurs in nanocrystalline materials.

Funding

The authors gratefully acknowledge the funding received from Stiftung ME Saar, Germany.

CRediT authorship contribution statement

Florian Schaefer: Conceptualization, Data curation, Formal analysis, Methodology, Project administration, Resources, Software, Supervision, Validation, Visualization, Writing – original draft, Funding acquisition. **Lukas Hasenfratz:** Investigation. **Rouven Schneider:** Data curation, Investigation, Methodology, Software, Visualization. **Christian Motz:** Formal analysis, Supervision, Writing – review & editing.

Declaration of competing interest

The authors declare that they have no known competing financial interests or personal relationships that could have appeared to influence the work reported in this paper.

References

[1] Johnson WH. On some remarkable changes produced in iron and steel by the action of hydrogen and acids. Nature 1875;11(281):393.
[2] Gerberich WW, Chen Y. Hydrogen-controlled cracking—An approach to threshold stress intensity. Metall Trans A 1975;6:271–8.
[3] Oriani R. Hydrogen embrittlement of steels. Annu Rev Mater Sci 1978;8(1):327–57.
[4] Hirth JP. Effects of hydrogen on the properties of iron and steel. Metall Trans A 1980;11:861–90.
[5] Oriani R. A mechanistic theory of hydrogen embrittlement of steels. Ber Bunsenges Phys Chem 1972;76(8):848–57.
[6] Vehoff H, Rothe W. Gaseous hydrogen embrittlement in FeSi-and Ni-single crystals. In: Perspectives in hydrogen in metals. Elsevier; 1986, p. 647–59.
[7] Birnbaum HK, Sofronis P. Hydrogen-enhanced localized plasticity—a mechanism for hydrogen-related fracture. Mater Sci Eng A 1994;176(1–2):191–202.
[8] Kirchheim R. On the solute-defect interaction in the framework of a defactant concept. Int J Mater Res 2009;100(4):483–7.
[9] Kirchheim R. Revisiting hydrogen embrittlement models and hydrogen-induced homogeneous nucleation of dislocations. Scr Mater 2010;62(2):67–70.
[10] Barnoush A, Vehoff H. Recent developments in the study of hydrogen embrittlement: Hydrogen effect on dislocation nucleation. Acta Mater 2010;58(16):5274–85.
[11] Beachem CD. A new model for hydrogen-assisted cracking (hydrogen "embrittlement"). Metall Mater Trans B 1972;3:441–55.
[12] Kimura H, Matsui H. Reply to "further discussion on the lattice hardening due to dissolved hydrogen in iron and steel" by Asano and Otsuka. Scr Metall 1979;13(3):221–3.
[13] Vlasov N, Zaznoba V. The effect of hydrogen atoms on the mobility of edge dislocations. Phys Solid State 1999;41:404–6.
[14] Teter D, Robertson I, Birnbaum H. The effects of hydrogen on the deformation and fracture of β-titanium. Acta Mater 2001;49(20):4313–23.
[15] Rao J, Lee S, Dehm G, Duarte MJ. Hardening effect of diffusible hydrogen on BCC Fe-based model alloys by in situ backside hydrogen charging. Mater Des 2023;232:112143.
[16] Song J, Curtin W. Mechanisms of hydrogen-enhanced localized plasticity: an atomistic study using α-Fe as a model system. Acta Mater 2014;68:61–9.
[17] Barrera O, Bombac D, Chen Y, Daff T, Galindo-Nava E, Gong P, Haley D, Horton R, Katzarov I, Kermode JR, et al. Understanding and mitigating hydrogen embrittlement of steels: a review of experimental, modelling and design progress from atomistic to continuum. J Mater Sci 2018;53(9):6251–90.
[18] Itakura M, Kaburaki H, Yamaguchi M, Okita T. The effect of hydrogen atoms on the screw dislocation mobility in bcc iron: A first-principles study. Acta Mater 2013;61(18):6857–67.
[19] Katzarov IH, Pashov DL, Paxton AT. Hydrogen embrittlement I. Analysis of hydrogen-enhanced localized plasticity: Effect of hydrogen on the velocity of screw dislocations in α-Fe. Phys Rev Mater 2017;1(3):033602.
[20] Gong P, Katzarov IH, Nutter J, Paxton AT, Rainforth WM. The influence of hydrogen on plasticity in pure iron—theory and experiment. Sci Rep 2020;10(1):10209.
[21] Murakami Y, Kanezaki T, Mine Y. Hydrogen effect against hydrogen embrittlement. Metall Mater Trans A 2010;41:2548–62.
[22] Mine Y, Olive J-M, Nagata K, Mitsutani T. Hydrogen effect on cyclic plasticity and crack growth in coarse-grained iron. Mater Sci Eng A 2011;528(28):8090–9.
[23] Schaefer F, Geyer S, Motz C. How hydrogen affects the formation and evolution of persistent slip bands in high-purity α-iron. Adv Energy Mater 2023;25(15):2201932.
[24] Zhao Y, Seok M-Y, Choi I-C, Lee Y-H, Park S-J, Ramamurty U, Suh J-Y, Jang J-i. The role of hydrogen in hardening/softening steel: Influence of the charging process. Scr Mater 2015;107:46–9.
[25] Wang M, Akiyama E, Tsuzaki K. Effect of hydrogen on the fracture behavior of high strength steel during slow strain rate test. Corros Sci 2007;49(11):4081–97.
[26] ISO 7539-9:2021, Corrosion of metals and alloys, Stress corrosion testing, Part 9: Preparation and use of pre-cracked specimens for tests under rising load or rising displacement, 2021, ISO TC156, DIN, ISO TC156.
[27] Momotani Y, Shibata A, Terada D, Tsuji N. Effect of strain rate on hydrogen embrittlement in low-carbon martensitic steel. Int J Hydrog Energy 2017;42(5):3371–9.
[28] Wang S. Hydrogen effect on dislocation motion in Fe and Ferritic alloys. 2013, http://dx.doi.org/10.14943/doctoral.k11124.
[29] Ferreira P, Robertson I, Birnbaum H. Hydrogen effects on the interaction between dislocations. Acta Mater 1998;46(5):1749–57.
[30] Abraham DP, Altstetter CJ. The effect of hydrogen on the yield and flow stress of an austenitic stainless steel. Metall Mater Trans A 1995;26:2849–58.
[31] Ebner AS, Plesiutschnig E, Clemens H, Pippan R, Maier-Kiener V. Rate-depending plastic deformation behaviour in a nickel-base alloy under hydrogen influence. Int J Hydrog Energy 2021;46(76):38132–43.
[32] Seeger A. LXV. On the theory of the low-temperature internal friction peak observed in metals. Phil Mag 1956;1(7):651–62.
[33] Narayanan S, McDowell DL, Zhu T. Crystal plasticity model for BCC iron atomistically informed by kinetics of correlated kinkpair nucleation on screw dislocation. J Mech Phys Solids 2014;65:54–68.
[34] Wang S, Hashimoto N, Ohnuki S. Effects of hydrogen on activation volume and density of mobile dislocations in iron-based alloy. Mater Sci Eng A 2013;562:101–8.
[35] Sirois E, Birnbaum H. Effects of hydrogen and carbon on thermally activated deformation in nickel. Acta Metall Mater 1992;40(6):1377–85. http://dx.doi.org/10.1016/0956-7151(92)90438-K.
[36] Schüler K, Philippi B, Weinmann M, Marx VM, Vehoff H. Effects of processing on texture, internal stresses and mechanical properties during the pulsed electrodeposition of nanocrystalline and ultrafine-grained nickel. Acta Mater 2013;61(11):3945–55.
[37] Mohanty G, Wehrs J, Boyce BL, Taylor A, Hasegawa M, Philippe L, Michler J. Room temperature stress relaxation in nanocrystalline Ni measured by micropillar compression and miniature tension. J Mater Res 2016;31(8):1085–95.

[38] Maier V, Durst K, Mueller J, Backes B, Höppel HW, Göken M. Nanoindentation strain-rate jump tests for determining the local strain-rate sensitivity in nanocrystalline Ni and ultrafine-grained Al. J Mater Res 2011;26(11):1421–30.
[39] Maier-Kiener V, An X, Li L, Zhang Z, Pippan R, Durst K. Influence of solid solution strengthening on the local mechanical properties of single crystal and ultrafine-grained binary Cu–Al *X* solid solutions. J Mater Res 2017;32(24):4583–91. http://dx.doi.org/10.1557/jmr.2017.320.
[40] Prasad K, Balaji V, Krishnaswamy H, Phani PS, Carlone P. Rigorous analysis and pragmatic guidelines in estimating strain rate sensitivity using stress relaxation test. Mech Mater 2022;168:104279. http://dx.doi.org/10.1016/j.mechmat.2022.104279.
[41] Seeger A. Report of a conf. on defects in crystalline solids. Tech. rep., London: The Physical Society; 1954, p. 391.
[42] Vehoff H, Lemaire D, Schüler K, Waschkies T, Yang B. The effect of grain size on strain rate sensitivity and activation volume–from nano to ufg nickel. Int J Mater Res 2007;98(4):259–68.
[43] Lucas B, Oliver W. Indentation power-law creep of high-purity indium. Metall Mater Trans A 1999;30:601–10.
[44] Maier V, Hohenwarter A, Pippan R, Kiener D. Thermally activated deformation processes in body-centered cubic Cr–how microstructure influences strain-rate sensitivity. Scr Mater 2015;106:42–5.
[45] Wehrs J, Mohanty G, Guillonneau G, Taylor AA, Maeder X, Frey D, Philippe L, Mischler S, Wheeler JM, Michler J. Comparison of in situ micromechanical strain-rate sensitivity measurement techniques. JOM 2015;67:1684–93.
[46] Alkorta J, Martínez-Esnaola JM, Sevillano JG. Critical examination of strain-rate sensitivity measurement by nanoindentation methods: Application to severely deformed niobium. Acta Mater 2008;56(4):884–93.
[47] Mayo M, Nix W. A micro-indentation study of superplasticity in Pb, Sn, and Sn-38 wt% Pb. Acta Metall 1988;36(8):2183–92.
[48] Sakai M, Akatsu T, Numata S, Matsuda K. Linear strain hardening in elastoplastic indentation contact. J Mater Res 2003;18(9):2087–96.
[49] Leitner A, Maier-Kiener V, Kiener D. Essential refinements of spherical nanoindentation protocols for the reliable determination of mechanical flow curves. Mater Des 2018;146:69–80.
[50] Zhao Y, Park J-M, Lee D-H, Song EJ, Suh J-Y, Ramamurty U, Jang J-i. Influences of hydrogen charging method on the hydrogen distribution and nanomechanical properties of face-centered cubic high-entropy alloy: A comparative study. Scr Mater 2019;168:76–80.
[51] Drexler A, Bergmann C, Manke G, Kokotin V, Mraczek K, Leitner S, Pohl M, Ecker W. Local hydrogen accumulation after cold forming and heat treatment in punched advanced high strength steel sheets. J Alloys Compd 2021;856:158226.
[52] Müller C, Zamanzade M, Motz C. The impact of hydrogen on mechanical properties; a new in situ nanoindentation testing method. Micromachines 2019;10(2):114.
[53] Luksch J, Lambai A, Mohanty G, Schaefer F, Motz C. Bridging macro to micro-scale fatigue crack growth by advanced fracture mechanical testing on the meso-scale. Mater Sci Eng A 2023;884:145452.
[54] Hajilou T, Hope MS, Zavieh AH, Kheradmand N, Johnsen R, Barnoush A. In situ small-scale hydrogen embrittlement testing made easy: An electrolyte for preserving surface integrity at nano-scale during hydrogen charging. Int J Hydrog Energy 2018;43(27):12516–29.
[55] Volpp T, Göring E, Kuschke W-M, Arzt E. Grain size determination and limits to hall-petch behavior in nanocrystalline NiAl powders. Nanostruct Mater 1997;8(7):855–65.
[56] Dalla Torre F, Spätig P, Schäublin R, Victoria M. Deformation behaviour and microstructure of nanocrystalline electrodeposited and high pressure torsioned nickel. Acta Mater 2005;53(8):2337–49. http://dx.doi.org/10.1016/j.actamat.2005.01.041.
[57] Gu C, Lian J, Jiang Q, Zheng W. Experimental and modelling investigations on strain rate sensitivity of an electrodeposited 20 nm grain sized Ni. J Phys D: Appl Phys 2007;40(23):7440.
[58] Wang YM, Hamza AV, Ma E. Activation volume and density of mobile dislocations in plastically deforming nanocrystalline Ni. Appl Phys Lett 2005;86(24):241917. http://dx.doi.org/10.1063/1.1946899.
[59] Vercruysse F, Claeys L, Depover T, Verbeken K, Verleysen P, Petrov R. The effect of Nb on the high strain rate hydrogen embrittlement of Q&P steel. In: EPJ web of conferences. Vol. 250, EDP Sciences; 2021, p. 03007.